Interaction of Helium Rydberg State Atoms with Superfluid Helium

Steven L. Fiedler · Jussi Eloranta

Abstract The pair potentials between ground state helium and Rydberg He*$(2s, 2p, 3s)$ atoms are calculated by the full configuration interaction electronic structure method for both the electronic singlet and the triplet manifolds. The obtained pair potentials are validated against existing experimental molecular and atomic data. Most states show remarkable energy barriers at long distances ($R > 5$ Å), which can effectively stabilize He* against the formation of He$_2^*$ at low nuclear kinetic energies. Bosonic density functional theory calculations, based on the calculated pair potential data, indicate that the triplet ground state He* reside in spherical bubbles in superfluid helium with a barycenter radius of 6.1 Å at the liquid saturated vapor pressure. The pressure dependency of the relative He* $2s\,^3S \rightarrow 2p\,^3P$ absorption line blue shift in the liquid was obtained through both the statistical line broadening theory as well as the dynamic adiabatic following method. The pronounced difference between the results from the static and dynamic models is attributed to the dynamic Jahn–Teller effect that takes places in the electronically excited state within the dephasing time of 150 fs. Transient non-thermalized liquid surroundings near He* may contribute to an artificial reduction in the absorption line blue shift by up to 30 cm^{-1}.

Keywords Excited state helium · Liquid helium · Optical spectroscopy

S. L. Fiedler
Department of Chemistry, Pomona College, Chemistry,
645 N. College Avenue, Claremont, CA 91711, USA

J. Eloranta (✉)
Department of Chemistry and Biochemistry, California State University at Northridge,
18111 Nordhoff St., Northridge, CA 91330, USA
e-mail: Jussi.Eloranta@csun.edu

 Springer

1 Introduction

When liquid helium is excited by a high-energy process, such as electron bombardment, radioactive source or vacuum ultraviolet radiation, excited helium atoms (He*) and molecular excimers (He$_2^*$) are formed [1–8]. The nascent excited electronic singlet states decay rapidly on a nanosecond time scale through spontaneous emission to the electric dipole allowed ground state, while the triplet states are metastable due to the lack of significant source of spin-orbit coupling [1,5]. The lifetime of He$_2^*$ in liquid helium has been measured as 13 s whereas for He* this is only 15 μs despite of its long lifetime in the gas phase, 8,000 s [9–11]. When helium is ionized, the direct electron $-$He$^+$ recombination may lead to the generation of excited triplet state helium atoms He* (e.g., 2^3S, 2^3P, etc.) and, provided that, the corresponding He*–He coordinate is accessible, triplet state molecular excimers (He$_2^*$) may also form [4,5]. Alternatively, if the charges separate as He$^+$ and e^- in the liquid, the positive ion will directly react with a nearby ground state He atom to first form He$_2^+$ and then later recombine with the electron to form triplet state He$_2^*$. While the outcome of these two different mechanisms is the same, there is an important difference in the dissipation of the electron kinetic energy. In the former case the "hot electron" dissipates its excess energy immediately by heating the surroundings of the He$_2^*$ formed whereas in the latter case the electron will first lose its energy through collisions with neutral He atoms in the liquid and the eventual "cold electron" $-$He$_2^+$ recombination will then release a minimal amount of energy into the immediate neighborhood of the excimer formed. The cold electron technique has been used, for example, to produce properly thermalized He$_2^*$ molecules for spectroscopic measurements in bulk superfluid helium [12,13].

Both optical absorption and fluorescence spectroscopic techniques have been used to study the coupling between He*/He$_2^*$ and the surrounding liquid helium bath [4,5,2, 3,12,13]. In both experimental arrangements the resulting line shifts and broadening are sensitive to the liquid structure around the absorbing/emitting species. In most cases the changes in absorption line profiles are more pronounced than by fluorescence because of the typically steeper repulsive excited state potential with the surrounding helium. Thus absorption lines tend to exhibit significant blue shifting and broadening whereas fluorescence lines often remain close to their gas phase origin. There are exceptions to the latter case, for example, when the excited state repulsive potential is very weak and the surrounding bath can sample this region efficiently as a function of external pressure [14]. Absorption measurements have demonstrated that the triplet state atomic He*($2s\ ^3S$) and molecular He$_2^*$($a\ ^3\Sigma_u$) species are the most persistent forms of excitation in bulk superfluid helium. The molecular excimers display various absorption bands within its Rydberg electronic manifold whereas only one atomic He* absorption line corresponding to the $2s\ ^3S \rightarrow 2p\ ^3P$ transition has been reported in the literature [5]. In addition to the slow radiative decay, destruction of the solvated He* atoms may also occur through He* + He → He$_2^*$ or He* + He* → He$_2^*$ annihilation. The previous theoretical calculations of He*($2s\ ^3S$) and He$_2^*$(^3a) solvation in superfluid helium have established that they reside in spherical bubbles with the barycenter radii varying between 5 and 7 Å [15–18]. Such bubbles are much smaller than that of solvated electrons, which have a radius of *ca.* 18.5 Å [19–21].

The first spectroscopic experiments for the He* $2s\,^3S$–$2p\,^3P$ transition were carried out by Soley and Fitzsimmons [22] and Walters et al. [3] by bombarding bulk superfluid helium with a 160 keV electron beam. Under liquid saturated vapor pressure (SVP) conditions at 1.7 K the absorption line was assigned to be within 5 cm^{-1} of the corresponding gas phase value. While this shift is unusually small considering the relatively large change in the effective size of the atomic He* Rydberg orbitals involved in the transition, the subsequent theoretical bubble model calculations appeared to provide satisfactory agreement with the experiment [15]. However, it should be noted that this model involves various adjustable parameters for describing superfluid helium (e.g., surface tension, the liquid density trial function, the surface kinetic energy term) as well as the parameters describing the electronic structure degrees of freedom for He* (e.g., the choice of electronic wavefunction, electron–helium pseudopotential) and as such it must rely heavily on calibration with the available experimental data. To demonstrate this point, such calculations at SVP with an alternative liquid distribution function gave a blue shift of 118 cm^{-1}, which is much larger than the accepted bubble model result of 5 cm^{-1} [15]. The corresponding fluorescence line exhibited a red shift of *ca.* 30 cm^{-1} as compared to the gas phase line position, which was interpreted to originate from a non-spherical bubble geometry in the excited $2p\,^3P$ state [15]. The removal of the *p*-orbital degeneracy was proposed to arise by a dynamic Jahn–Teller (JT) effect where the symmetry is broken by the surrounding liquid.

In a related set of experiments on molecular He$_2^*$ excimer, analysis of the $^3a \rightarrow\,^3c$ absorption line profiles revealed significant differences depending on which technique was used for preparing the excimers [3,5,12,13]. Specifically, the cold electron technique [12] produced more pronounced blue shifts for the absorption band than the high energy electron bombardment [5] (150 vs. 100 cm^{-1}). The cold electron emission spectra agree withing 5 cm^{-1} with the results from combined theoretical bosonic density functional theory (DFT) and ab initio calculations [16]. Since the band shifts appear to depend on the method used for preparing the excimers, the two techniques must create different solvation environments for He$_2^*$. The high-energy electron bombardment method produces a smaller blue shift, which corresponds to a reduced liquid density around the excimer as compared to the cold electron technique. The same effect has also been observed for He* $2p\,^3P \leftarrow 3s\,^3S$ fluorescence line in liquid helium when Corona discharge was used to produce the excited helium atoms [14]. In this case, no apparent difference in the fluorescence line shifts between the 4.2 K measurements and the previous experiments in the superfluid phase at 1.8 K was observed even though the equilibrium liquid densities are very different at these temperatures (0.125 g cm^{-3} at 4.2 K and 0.145 g cm^{-3} at 1.8 K) [14,22,23]. Therefore it was proposed that the heat dissipated near the absorber/emitter may introduce an artificial reduction of the blue shift for the experimentally observed line positions [14]. Furthermore, it was recently shown that thermal perturbations created in superfluid helium can have lifetimes extending up to the millisecond timescale [24], which may imply that He*/He$_2^*$ require long times for proper thermalization in the superfluid phase.

In this work, we first carry out high-level ab initio electronic structure calculations to obtain the relevant He$_2^*$ potential energy curves and validate them against the existing high resolution spectroscopic data. To characterize pressure dependent He* solvation

structures in bulk superfluid helium, we perform bosonic DFT calculations that employ our new ab initio data. The resulting liquid density profiles are then used to model the He* $2s\,^3S \rightarrow 2p\,^3P$ optical absorption spectrum as a function of external pressure. The origin of the absorption line shift (i.e., thermal effects and dynamic liquid response due to JT) is discussed based on the theoretical results.

2 Theory

The He*–He interaction was computed at the full configuration interaction (FCI) level using the two basis sets specified in the Appendix. To demonstrate the ability of the present basis sets to describe the relevant excited states, the absolute helium atom excitation energies are also listed in Table 1. The FCI method is size consistent and as such it allows for the accounting of the basis set superposition error (BSSE) through the counterpoise correction of Boys and Bernardi [25]. The calculations were carried out within D_{2h} point group except when the symmetry was naturally lowered to C_{2v} by the use of dummy atomic centers during the BSSE correction. At the atomic limits, the calculated excited states correlated with the $2s$, $2p_{x,y,z}$ and $3s$ asymptotes. All the electronic structure calculations were conducted with the parallel version of MOLPRO code [26,27]. The harmonic and anharmonic frequencies were obtained by first solving the diatomic vibrational problem numerically for the given potential and then fitting the resulting eigenvalues to a polynomial expansion yielding the quantities of interest. Note that the present potentials possess rather large anharmonicities and therefore even the experimentally obtained values are very sensitive to the number of vibronic lines used in obtaining the frequencies.

The bosonic DFT calculations employed the Orsay–Trento (OT) functional, which has been demonstrated to reproduce the bulk liquid properties (e.g., the dispersion relation) and to accurately model pure and doped helium droplets as well as impurities embedded in bulk superfluid helium [28–30]. An extended version of the OT functional was used in this study, which allows it to describe liquid helium at non-zero temperatures [31]. The interaction of He* with liquid helium was included in this model through the following energy functional:

$$E\left[\psi', \psi\right] = \int \int \left|\psi'(R)\right|^2 V(|R - r|) \left|\psi(r)\right|^2 d^3r d^3R \qquad (1)$$

where ψ' is the He* nuclear wavefunction localized inside the bubble, ψ is the liquid helium order parameter and V represents the He*–He pair potential. By using the

	State	Basis set '*'	Basis set '**'	Atomic calculation [45]	Experimental data [46]
Table 1 Comparison of absolute excitation energies (cm^{-1}) of the lowest He* triplet states for the applied basis sets	1s2s	159,410.9	159,448.8	159,886.2	159,856.0
	1s2p	168,797.5	168,691.6	169,118.4	169,086.8
	1s3s	182,799.2	182,825.8	183,269.1	183,236.8

least action principle, the OT functional can be formulated as a time-dependent non-linear Schrödinger equation [32]. The numerical solution for this problem in 3-D can be obtained by employing the Crank–Nicolson method combined with the operator splitting technique [33,34]. A $256 \times 256 \times 256$ Cartesian grid with a 0.2 Å spatial step was employed for both grids representing the liquid and He*. To obtain the ground state solution for the liquid, the time-dependent OT equation was propagated in imaginary time [33]. Typically a time step of 50 fs (5 fs for real time dynamics calculations), and 200 iterations were sufficient to reach the convergence. During the imaginary time iterations, the total liquid energy was also calculated by numerically integrating the OT energy density to observe the convergence of the method. The zero-point (ZP) motion for He* was included in the calculations by propagating both the liquid and He* wavefunctions simultaneously with the coupling given by the convoluted He*–He pair potential in Eq. (1).

The time domain description is often the most appropriate approach for analyzing spectroscopic transitions in condensed medium [35]. The linear dipolar absorption spectrum between two states can be obtained from the corresponding time correlation function through Fourier transformation. As the time correlation function depends on the time evolution of the full quantum system, it is not possible to evaluate it directly from the DFT order parameter because the true many-body wavefunction is not available. In this work, we have used two different methods for evaluating the absorption spectrum: (1) statistical pressure broadening model (Anderson model) [36,15,16] and (2) the adiabatic following method [16,37]. In the statistical pressure broadening model the time correlation function $c(t)$ is written in terms of the equilibrium liquid density around ground state He*:

$$ c(t) = \exp \left\{ - \int \int \left[1 - \exp \left(- \frac{i \Delta V_{eg} \left(|R - r| \right) t}{\hbar} \right) \right] \rho'_g(R) \rho_g(r) d^3 r d^3 R \right\} \quad (2) $$

where ρ_g is the equilibrium liquid density, ρ'_g is the He* ZP density inside the solvation cavity and $\Delta V_{eg} = V_e - V_g$ is the difference between the ground (V_g) and excited (V_e) state He*–He potentials. For broad structureless lines, when electronic dephasing due to the continuum of frequencies present in the difference potential dominates, the statistical limit is usually sufficient to provide a robust approach based on only the ground state liquid density. However, if the dephasing is slow relative to the bath dynamics, the time-dependent liquid response may also contribute to the absorption spectrum as evidenced by, for example, the observation of the accompanying roton/maxon sidebands in helium droplets [38,39].

The adiabatic following method assumes a two-level system (i.e., ground and excited electronic states), which is subject to a slowly varying external perturbation induced by the surrounding bath. It can be shown that for a dipolar transition employing the rotating frame approximation, the first-order polarization $P^{(1)}(t)$ can be written as [39,37]:

$$ P^{(1)}(t) \propto i \int_0^t \exp \left(- \frac{i}{\hbar} \int_{t'}^t E_{ext}(t'') dt'' - i \omega t' \right) dt' + C.C. \quad (3) $$

Fig. 1 Overview of the potential energy curves for He*(2s, 2p, 3s)—He in the electronic triplet state manifold from FCI calculations using the '*' basis set specified in the Appendix. (Color figure online)
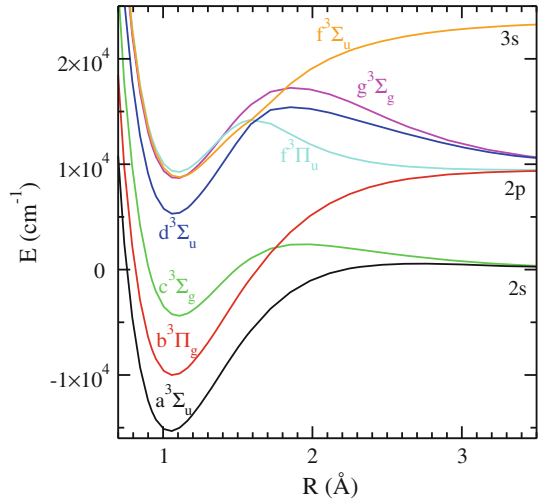
where $C.C.$ stands for complex conjugate of the preceding term and $E_{ext}(t)$ is the difference between the bath–system interaction energies for the ground and excited electronic states:

$$
E_{ext}(t) = \int\int \rho_e'(R,t)V_e(|R-r|)\rho_e(r,t)d^3r d^3R
$$
$$
- \int\int \rho_g'(R)V_g(|R-r|)\rho_g(r)d^3r d^3R \tag{4}
$$

Note that the ground state density ρ_g is time independent and corresponds to the initial liquid density around He* but ρ_e requires real time evolution of the system on the excited state. Equation (3) does not include dephasing, which can be empirically included through a decaying exponential:

$$
\bar{P}^{(1)}(t) = e^{-t/\tau}P^{(1)}(t), \tag{5}
$$

where τ represents the dephasing time constant for the system. Essentially, this value controls the time the excited state dynamics contributes to the lineshape. If τ is short, a structureless broad line is observed whereas for a large value of τ discrete structure due to the bath dynamics may appear [39]. The linear absorption spectrum can finally be obtained through Fourier transformation of Eq. (5).

To model the He* $2s\,^3S \rightarrow 2p\,^3P$ absorption spectrum, the relevant diatomic molecular states contributing to the transition must be identified. As shown in Fig. 1 the molecular states correlating with the $2s$ asymptote are $a^3\Sigma_u$ and $c^3\Sigma_g$, which both have essentially identical long-range behavior ($R > 4$ Å; see also Fig. 2). Thus, in the atomic regime, either the ^3a or ^3c state potential can be chosen to represent the electronic ground state in the DFT calculations. For the He* $2p\,^3P$ state, four different diatomic molecular states may contribute to the perturbed atomic absorption
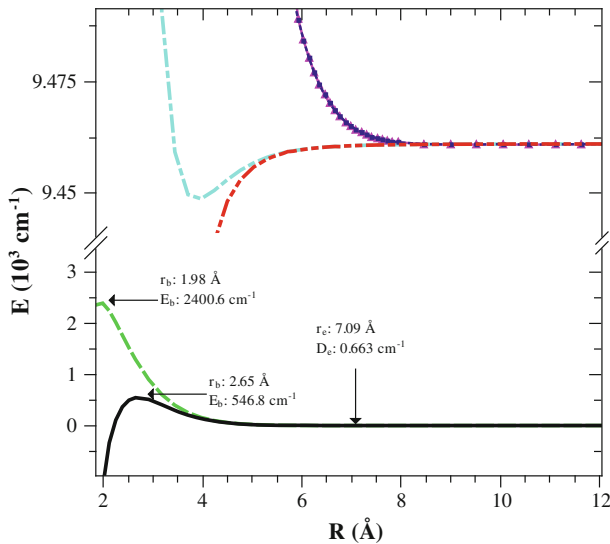
Fig. 2 Overview of the potential energy curves for He*$(2s, 2p)$–He in the electronic triplet state manifold at $R > 2$ Å. The continuous *black curve* corresponds to the $a^3\Sigma_u$ state, the *dashed green curve* to the $c^3\Sigma_g$ state, the *red dot-dot-dash curve* to the $b^3\Pi_g$ state, the *light blue dash-dot-dash line* to the $f^3\Pi_u$, *magenta triangles* to the $g^3\Sigma_g$ and *dark blue dots* to the $d^3\Sigma_u$ state. The recombination barriers for the states correlating with the $2s$ asymptote are also indicated along with the local minimum around 7.1 Å indicated by an *arrow*. The data shown corresponds to FCI calculations with the '*' basis set specified in the Appendix. (Color figure online)

spectrum: $b^3\Pi_g$, $d^3\Sigma_u$, $f^3\Pi_u$ and $g^3\Sigma_g$. As shown in Fig. 2, the $\Sigma_{g/u}$ as well as the $\Pi_{g/u}$ states have identical long-range behavior (i.e., the system has not yet entered the molecular regime). Thus only two states, ^3g (the Rydberg p orbital along the molecular axis z) and ^3b (the Rydberg p orbital perpendicular to the molecular axes; x and y components), need to be considered for the excited state. The DFT calculations employed the pair potentials obtained using the '**' basis defined in the Appendix.

3 Results and Discussion

The singlet and triplet potential energy curves (PECs) of He$_2^*$ for the states correlating with $2s$, $2p$ and $3s$ atomic asymptotes are shown in Figs. 1 and 3 with the derived and literature values for the spectroscopic constants collected in Tables 2 and 3. Note that the ground triplet Rydberg state ($a\,^3\Sigma_u$) is metastable and can therefore be conveniently accessed by optical spectroscopy experiments. The general shape of the calculated PECs for both singlet and triplet states is in agreement with the previously published data [17,40,41] but through the improved treatment of electron correlation and the extended basis set, we have been able to obtain new theoretical estimates for the equilibrium bond lengths, harmonic frequencies, anharmonic frequencies and especially accurate energetics at large inter atomic distances (see Tables 2, 3). For the low-lying molecular singlet and triplet states the absolute electronic ori-

Fig. 3 Overview of the potential energy curves for He*($2s$, $2p$, $3s$)–He in the electronic singlet state manifold from FCI calculations using the '*' basis set specified in the Appendix. (Color figure online)
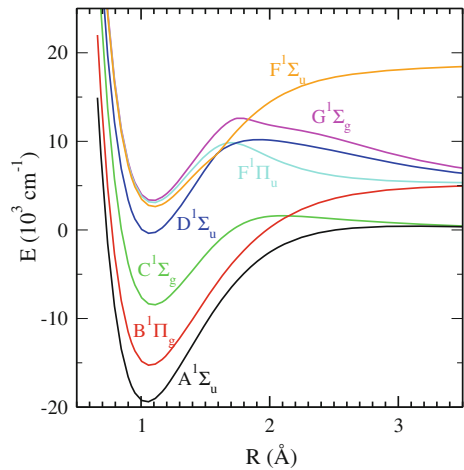

Table 2 Spectroscopic constants for He$_2^*$ singlet states in comparison to experimentally determined values

State	Ref.	r_e (Å)	ω_e (cm^{-1})	$\omega_e x_e$ (cm^{-1})	T_e (cm^{-1})
A ($^1\Sigma_u$)	[47]	1.04	1,861	35	146,354
	*	1.1	1,850	37	146,248
B ($^1\Pi_g$)	[48]	1.07	1,766	35	149,914
	[49]	1.07	1,766	34	149,914
	*	1.06	1,753	36	150,378
C ($^1\Sigma_g$)	[48]	1.09	1,572	–	157,446
	[50]	1.09	1,653	41	157,416
	*	1.1	1,649	30	157,196
D ($^1\Sigma_u$)	[49]	1.07	1,746	36	165,086
	*	1.1	1,732	24	165,266
F ($^1\Pi_u$)	[51]	1.08	1,671	40	165,992
	*	1.1	1,624	24	168,739
F ($^1\Sigma_u$)	[52]	1.09	1,564	–	165,813
	*	1.1	1,591	54	168,417
G ($^1\Sigma_g$)	[53]	–	–	–	168,379
	*	1.1	1,644	19	168,988

Electronic term values, T_e, were derived from the referenced $\nu_{(0-0)}$ electronic transitions with accounting for zero point energies obtained from the usual vibrational energy-level expression: $G(v) = \omega_e(v+1/2) - \omega_e x_e(v+1/2)^2 + \dots$ and appended to T_e values from Ref. [52] for the A ($^1\Sigma_u$) state. The results obtained in this work for the applied basis sets are denoted by '*' and '**' (see Appendix)

gins are typically reproduced within 100–200 cm^{-1} from the experimental data (0.1 % absolute error) and the harmonic frequencies are within *ca.* 10 cm^{-1}. The analysis of the harmonic and anharmonic frequencies is complicated by the unusual shape of the PECs especially at long distances. For higher states (e.g., F/f, g/G) both electronic origins and harmonic frequencies deviate from the experimental data indicating

Table 3 Spectroscopic constants for He$_2^*$ triplet states in comparison to experimentally determined values

State	Ref.	r_e (Å)	ω_e (cm^{-1})	$\omega_e x_e$ (cm^{-1})	T_e (cm^{-1})
a ($^3\Sigma_u$)	[48]	1.045	1,809	38	144,048
	*	1.1	1,806	42	143,873
	**	1.047	1,799	–	144,375
b ($^3\Pi_g$)	[48]	1.065	1,769	35	148,835
	*	1.1	1,760	37	149,181
	**	1.069	1,744	–	149,197
c ($^3\Sigma_g$)	[48]	1.098	1,588	54	155,052
	*	1.1	1,584	60	154,803
	**	1.100	1,570	–	155,465
d ($^3\Sigma_u$)	[54]	1.071	1,728	36	164,479
	*	1.1	1,713	37	164,493
	**	1.079	1,644	–	164,794
f ($^3\Sigma_u$)	[51]	1.091	1,636	44	165,693
	*	1.1	1,561	57	167,959
f ($^3\Pi_u$)	[51]	1.086	1,661	45	165,897
	*	1.1	1,562	68	168,458
g ($^3\Sigma_g$)	[55]	1.080	1,672	–	–
	*	1.1	1,636	38	167,878
	**	1.090	1,663	–	168,066

Electronic term values, T_e, were derived from the referenced $\nu_{(0-0)}$ electronic transitions with accounting for zero point energies obtained from the usual vibrational energy-level expression: $G(v) = \omega_e(v + 1/2) - \omega_e x_e(v + 1/2)^2 + ...$ and appended to T_e values from reference [52] for the a ($^3\Sigma_u$) states. The results obtained in this work for the applied basis sets are denoted by '*' and '**' (see Appendix)

either a deficiency in the applied basis sets or problem with the spectroscopic data. As shown in Table 1, the calculated absolute atomic excitation energies lie generally within a few hundred cm^{-1} from the known atomic values indicating that the applied basis sets are sufficiently large to describe the corresponding molecular states accurately.

The long-range behavior for both the singlet and triplet states are emphasized in Figs. 2 and 4. The relatively high recombination barriers towards the diatomic excimer present in the ^3a and ^3c state PECs, with heights of 502 cm^{-1} (basis '**'; 550 cm^{-1} for basis '*') and 2,326 cm^{-1} (basis '**'; 2,410 cm^{-1} for basis '*'), respectively, protect He* against the formation of molecular He$_2^*$ at low temperatures. Note, however, that in most experimental arrangements, high energy processes are involved in generating such species, which may easily overcome these barriers resulting in the spontaneous formation of He$_2^*$. The states correlating with the atomic $2p$ asymptote (i.e., ^3b, ^3d, ^3f, ^3g) display interesting behavior [see Fig. (2)] as one of the states (^3b) shows no long-range recombination barrier and may therefore lead to direct formation of He$_2^*$ in the ^3b molecular state provided that the dynamic JT effect is able to split the degenerate atomic $2p$ orbitals. Thus an optical excitation of the $2s$ $^3S \rightarrow 2p$ ^3P transition may lead to partial destruction of the He* population through a photo

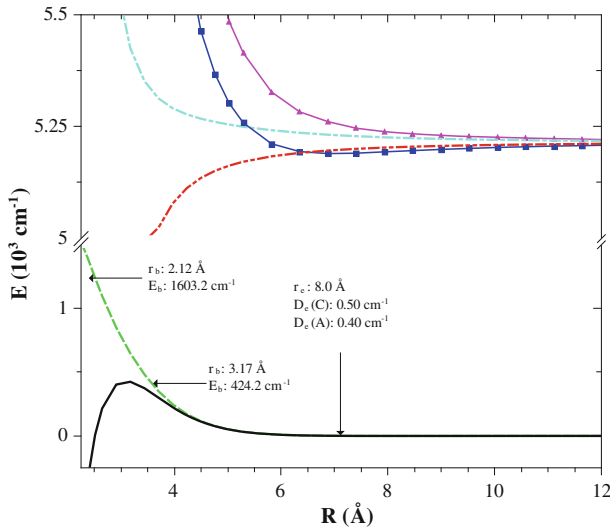**Fig. 4** Overview of the potential energy curves for He*$(2s, 2p)$–He in the electronic singlet state manifold at $R > 2$ Å using the '*' basis set (see Appendix). The continuous *black curve* corresponds to the $A^1\Sigma_u$ state, the *dashed green curve* to the $C^1\Sigma_g$ state, the *red dot-dot-dash curve* to the $B^1\Pi_g$ state, the *light blue dash-dot-dash line* to the $F^1\Pi_u$, *magenta triangles* to the $G^1\Sigma_g$ and *dark blue dots* to the $D^1\Sigma_u$ state. The recombination barriers for the states correlating with the $2s$ asymptote are also shown along with the local minimum around 8.0 Å indicated by an *arrow*. (Color figure online)

induced reaction to He$_2^*$. In the Rydberg atom picture, these molecular Σ and Π states correspond to the $2p$ orbital facing towards the approaching ground state helium atom and perpendicular to it, respectively. The long-range asymptotic region of the diatomic states correlating with He*$(2s)$ and He*$(2p)$ are important for modeling the He* $2s$ $^3S \rightarrow 2p\ ^3P$ transition in liquid helium (see Fig. 2).

In bulk superfluid helium, He* $2s\ ^3S$ forms a bubble state with the gas–liquid interface barycenter radius, R_b, depending weakly on the external pressure: $R_b = 6.1$ Å at SVP and $R_b = 5.7$ Å at 2.5 MPa ($T = 1.6$ K). Since the long-range region of the He*–He ground state potential is spherically symmetric, the bubble preserves the same symmetry. The pressure dependency of the liquid density profiles and the corresponding He* nuclear ZP densities are shown in Fig. 5. As the pressure increases, the interface becomes narrower and is slightly shifted towards He*. The oscillatory structure present in the profiles reflects the correlated nature of the liquid, which becomes more pronounced at high pressures for narrow interfaces. When the pressure is above SVP and $T \leq 3.0$ K, the direct effect of temperature on the density profiles appears to be very small with the main changes originating from the variations in bulk liquid density as a function of pressure and temperature rather than the ideal gas contribution or changes in the temperature dependent parameters of the extended OT functional.

The relative absorption line shifts are shown in Fig. 6 where the results using Eq. (2) are given along with the experimental values. The static Anderson model not only produces excessively large blue shifts but also overshoots the shift vs. pressure slope.

Fig. 5 Calculated liquid helium density profiles and He* ZP density as a function of external pressure at 1.6 K. (Color figure online)
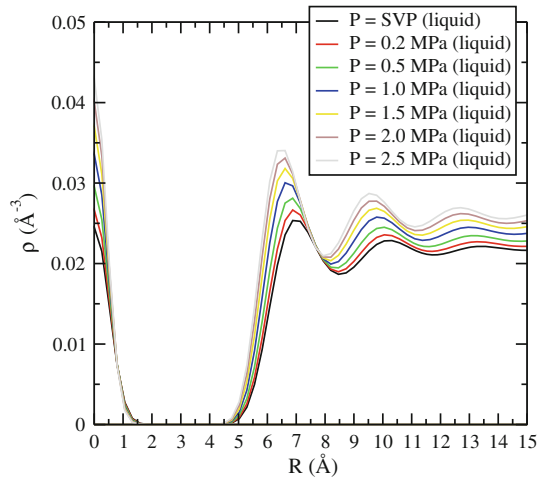

Fig. 6 Relative shifts in the 2s $^3S \to 2p\ ^3P$ absorption lines as a function of external pressure. The data shown corresponds to the experimental points (*circles*) [22,15], static treatment of Eq. (2) with (*pluses*) and without (*diamonds*) the He* ZP motion included, and the dynamic treatment of Eq. (3) with $\tau = 100, 150, 200$ fs (*stars*, *crosses* and *squares*, respectively). The adiabatic following calculations included the ZP motion for He*. (Color figure online)
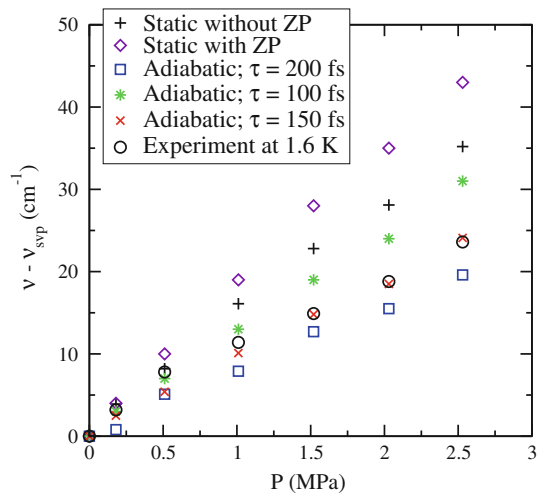
If the experimental data points are horizontally extrapolated to the calculated values on the left in Fig. 6, the hypothetical local pressure reduction would range from zero up to 1.5 MPa. This greatly exceeds the previously observed value for He* $2p\ ^3P \leftarrow 3s\ ^3S$ fluorescence line where the constant 0.5 MPa difference between experiment and theory was proposed to originate from a local increase in temperature around He* [14]. Furthermore, in that study, the slope of the experimental versus calculated pressure induced shifts were identical, which is clearly not the case here (cf. Fig. 6). Thus, in the present case, some other mechanism, which is not included in the Anderson theory [Eq. (2)], must be contributing to the reduction in the experimentally observed shift versus pressure slope. In this model the overall line shift depends on the difference between the ground and excited state solvation energies in the static ground state bubble geometry.

One plausible explanation for the overestimation of the $2s\,^3S \rightarrow 2p\,^3P$ absorption line shift by the Anderson model is the reduction of the He*–bath interaction energy due to the excited state solvation dynamics (i.e., dynamic JT). By inspecting the He*$(2p)$–He pair potential in Fig. 2, it is clear that the equilibrium liquid density distribution around the $2s\,^3S$ state will experience significant interaction through the difference potential upon excitation to $2p\,^3P$. This is in contrast with the fluorescence experiments in Ref. [14] where the initial state liquid density around $3s\,^3S$ was located far away from the strongly interacting region of the $2p\,^3P$ state and, consequently, the time for the liquid to penetrate the nodal region of the $2p$-orbital is fairly long, 3 ps [14]. The standard Anderson theory cannot account for the possible dynamics in the excited state and therefore the adiabatic following model of Eq. (3) was used to determine if the JT mechanism could explain the apparent discrepancy between the static theory and experiments. The results from the adiabatic following model calculations are shown in Fig. 6. The only adjustable parameter in the model is the dephasing time constant τ [see Eq. (5)], which essentially dictates how long period of the dynamics in the excited states will be included in the spectrum. Results for three different τ values 100, 150 and 200 fs are shown in Fig. 6 with the best match to the experimental data obtained for $\tau = 150$ fs. In the previous theoretical treatment of Ref. [15], an estimate of 250 fs was given for the dephasing time and the authors concluded that the excited state dynamics is not completely negligible in this time scale but it was not possible to include this contribution in their static lineshape calculation (Anderson model). Effectively, the overall blue shift is reduced by the decrease in the excited state bath interaction energy during the first 150 fs of the liquid evolution. Based on this result, we assign the reduced blue shifts observed in the experiments to arise from dynamic JT that takes place in the excited state. The calculated full-width-half-height (FWHM) linewidths range from 80 cm^{-1} at SVP to *ca.* 110 cm^{-1} at 2.5 MPa, which are very close to those observed experimentally [22,15]. The experimental data points that were given in Ref. [15] compare with our calculations as follows: (1) at $P = 0.07$ MPa the experiments give a FWHM linewidth of 83 cm^{-1} whereas our calculations give 90 cm^{-1}; (2) at $P = 1.0$ MPa these are 89 and 95 cm^{-1} and (3) at $P = 2.5$ MPa the linewidths are 103 and 110 cm^{-1}, correspondingly. Note that the absorption lines are asymmetric, which complicates the determination of the lineshape parameters. The calculated line profiles are displayed in Fig. 7 to show the overall lineshape as a function of pressure.

The remaining question is related to the absolute line origin of the He* $2s\,^3S \rightarrow 2p\,^3P$ transition. The experimental data suggests that the absorption line shift at SVP is close to zero (± 5 cm^{-1}) whereas the present theoretical calculations predict a blue shift of 30 cm^{-1}. This contribution is independent of pressure and has the same magnitude as the previously observed reduction in spectral line blue shifts due to the transient thermal effect. As discussed previously the He$_2^*$ ($^3a \rightarrow {}^3c$) absorption band, the reduction in blue shift due to this effect is 50 cm^{-1} and the corresponding reduction for the He* ($2p\,^3P \leftarrow 3s\,^3S$) fluorescence line is *ca.* 40 cm^{-1} [14]. Thus it is possible that the constant difference between the calculated and experimental line shifts (30 cm^{-1}) also originates from non-thermalized surroundings of He*, which is created by high energy electron bombardment. In this view, the effective 14 μs lifetime for triplet He* in liquid helium appears too short to allow for full thermalization. Finally,

Fig. 7 Calculated lineshapes at 1.6 K for the triplet He* $2s\,^3S$ $\rightarrow 2p\,^3P$ absorption line as obtained from Eq. (5) for the pressures indicated in the caption. The calculations included the ZP motion for He* inside the bubble. (Color figure online)
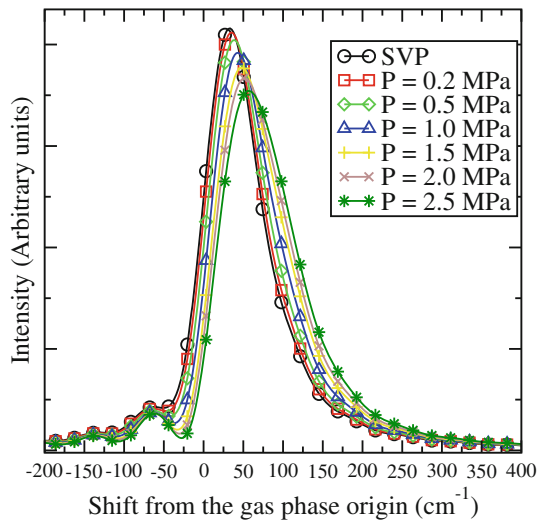
it should be noted that we cannot completely exclude the possibility of misassignment of the absolute SVP line origin in the experiments or an error in the He*–He pair potential such that it accidentally produces a constant offset in the evaluation of the line position.

Appendix

The small basis set denoted by '*' was augmented from that given in Ref. [42] by adding uncontracted diffuse gaussians with the exponents: s/0.04473, p/0.1280, d/0.2410 and f/0.4070. The large basis set, which is denoted by '**', was constructed according to Ref. [43] with selected d and f gaussians removed to avoid linear dependency problems in the molecular regime. The linearly dependent functions were identified by inspecting the lowest eigenstates of the overlap matrix [44]. For completeness, this basis set is specified in Table 4. To demonstrate the accuracy of these basis sets, absolute excitation energies for atomic He* are shown in Table 1.

Table 4 Gaussian basis set exponents for the basis denoted by '**'

Gaussian	Exponents																	
s	5×10^4	1×10^4	2×10^3	500	200	100	50	20	10	5	2	1	0.5	0.2	0.1	0.055	0.02	0.011	0.006
p							50	10	5	2	1	0.5	0.2	0.1	0.05	0.025	0.012	0.006
d										5				0.27	0.11	0.05		
f														0.6	0.09			

The basis set is fully uncontracted

References

1. A.V. Phelps, J. Phys. Rev. **99**, 1307 (1955)
2. W.S. Dennis, J.E. Durbin, W.A. Fitzsimmons, O. Heybey, G.K. Walters, J. Phys. Rev. Lett. **23**, 1083 (1969)
3. J.C. Hill, O. Heybey, G.K. Walters, Phys. Rev. Lett. **26**, 1213 (1971)
4. J.W. Keto, F.J. Soley, M. Stockton, W.A. Fitzsimmons, Phys. Rev. A **10**, 887 (1974a)
5. J.W. Keto, F.J. Soley, M. Stockton, W.A. Fitzsimmons, Phys. Rev. A **10**, 872 (1974b)
6. M. Stockton, J.W. Keto, W.A. Fitzsimmons, Phys. Rev. A **5**, 372 (1972)
7. K. von Haeften, A.R.B. de Castro, M. Joppien, L. Moussavizadeh, R. von Pietrowski, T. Möller, Phys. Rev. Lett. **78**, 4371 (1997)
8. T. Möller, K. von Haeften, R. von Pietrowski, Eur. Phys. J. D **9**, 5 (1999)
9. R. Golub, K. Habicht, Phys. Rev. A **59**, 20 (1999)
10. W. Keto, M. Stockton, W.A. Fitzsimmons, Phys. Rev. Lett. **28**, 792 (1972)
11. J.R. Woodworth, H.W. Moos, Phys. Rev. A **12**, 2455 (1975)
12. S.G. Kafanov, A.Y. Parshin, I.A. Todoshchenko, J. Exp. Theor. Phys. **91**, 991 (2000)
13. A.Y. Parshin, I.A. Todoshchenko, S.G. Kafanov, Physica B **284–288**, 91 (2000)
14. N. Bonifaci, F. Aitken, V.M. Atrazhev, S.F. Fielder, J. Eloranta, Phys. Rev. A **85**, 042706 (2012)
15. A.P. Hickman, N.F. Lane, Phys. Rev. B **12**, 3705 (1975)
16. J. Eloranta, N. Schwentner, V.A. Apkarian, J. Chem. Phys. **116**, 4039 (2002)
17. J. Eloranta, V.A. Apkarian, J. Chem. Phys. **115**, 752 (2001)
18. J. Eloranta, Chem. Phys. **332**, 304 (2007)
19. J. Eloranta, V.A. Apkarian, J. Chem. Phys. **117**, 10139 (2002)
20. D. Mateo, M. Pi, M. Barranco, Phys. Rev. B **81**, 174510 (2010)
21. W.B. Fowler, D.L. Dexter, Phys. Rev. **176**, 337 (1968)
22. F.J. Soley, W.A. Fitzsimmons, Phys. Rev. Lett. **32**, 988 (1974)
23. P.H. Zimmermann, J.F. Reichert, A.J. Dahm, Phys. Rev. B **15**, 2630 (1977)
24. E. Popov, M. Mammetkuliyev, J. Eloranta, J. Chem. Phys. **138**, 204307 (2013)
25. F. Boys, F. Bernardi, Mol. Phys. **19**, 553 (1970)
26. H.-J. Werner, P.J. Knowles, F.R. Manby, M. Schütz, P. Celani, G. Knizia, T. Korona, R. Lindh, A. Mitrushenkov, G. Rauhut, et al., Molpro, version 2010.1, a Package of ab initio Programs (2010), see http://www.molpro.net
27. P.J. Knowles, N.C. Handy, Chem. Phys. Lett. **111**, 315 (1984)
28. F. Dalfovo, A. Lastri, L. Pricaupenko, S. Stringari, J. Treiner, Phys. Rev. B **52**, 1193 (1995)
29. A. Hernando, M. Barranco, R. Mayol, M. Pi, F. Ancilotto, O. Bünermann, F. Stienkemeier, J. Low Temp. Phys. **158**, 105 (2010)
30. T. Kiljunen, L. Lehtovaara, H. Kunttu, J. Eloranta, Phys. Rev. A **69**, 012506 (2004)
31. F. Ancilotto, F. Faccin, F. Toigo, Phys. Rev. B **62**, 17035 (2000)
32. L. Lehtovaara, T. Kiljunen, J. Eloranta, J. Comp. Phys. **194**, 78 (2004)
33. L. Lehtovaara, J. Toivanen, J. Eloranta, J. Comp. Phys. **221**, 148 (2007)
34. J. Eloranta, A high-level library for managing 1-D, 2-D and 3-D regular grids, Available at http://www.sourceforge.net/projects/libgrid/ (2010)
35. S. Mukamel, *Principles of Nonlinear Optical Spectroscopy* (Oxford University Press, New York, 1995)
36. P.W. Anderson, Phys. Rev. **86**, 80 (1952)
37. L. Lehtovaara, J. Eloranta, J. Low Temp. Phys. **138**, 91 (2005)
38. M. Hartmann, F. Mielke, J.P. Toennies, A.F. Vilesov, G. Benedek, Phys. Rev. Lett. **76**, 4560 (1996)
39. J. Eloranta, H.Y. Seferyan, V.A. Apkarian, Chem. Phys. Lett. **396**, 155 (2004)
40. S.L. Guberman, W.A. Goddard, Phys. Rev. A **12**, 1203 (1975)
41. D. Vrinceanu, S. Kotochigova, H.R. Sadeghpour, Phys. Rev. A **69**, 022714 (2004)
42. K.K. Sunil, J. Lin, H. Siddiqui, P.E. Siska, K.D. Jordan, R. Shepard, J. Chem. Phys. **78**, 6190 (1983)
43. B. Deguilhem, Calcul ab initio d'observables pour les condensats d'hélium métastable (2009), http://books.google.com/books?id=SmRruAAACAAJ
44. A. Szabo, N.S. Ostlund, *Modern Quantum Chemistry: Introduction to Advanced Electronic Structure Theory* (Dover, New York, 1989)
45. D.C. Fowler, Q. Wu, G.W.F. Drake, Can. J. Phys. **84**, 83 (2006)
46. P.M. Laboratory, Atomic spectra database, Online database available at http://www.nist.gov/pml/data/asd.cfm (2013)

47. C. Brown, M. Ginter, J. Mol. Spectrosc. **40**, 302 (1971)
48. C. Focsa, P.F. Bernath, R. Colin, J. Mol. Spectrosc. **191**, 209 (1998)
49. M.L. Ginter, J. Mol. Spectrosc. **17**, 224 (1965a)
50. M.L. Ginter, J. Chem. Phys. **42**, 561 (1965b)
51. M.L. Ginter, J. Chem. Phys. **45**, 248 (1966)
52. K.P. Huber, G. Herzberg, *Molecular Spectra and Molecular Structure IV* (Reinhold, New York, Constants of Diatomic Molecules Van Nostrand, 1979)
53. D.S. Ginter, M.L. Ginter, J. Molec, J. Mol. Spectrosc. **138**, 29 (1989)
54. M.L. Ginter, J. Mol. Spectrosc. **18**, 321 (1965c)
55. F.B. Orth, M.L. Ginter, J. Mol. Spectrosc. **61**, 282 (1976)